NASA Technical Memorandum 86005 USAAVSCOM Technical Memorandum 84-A-9

An Experimental Investigation of the Parallel Blade-Vortex Interaction

F.X. Caradonna, G.H. Laub, and C. Tung

November 1984

National Aeronautics and Space Administration

United States Army Aviation Systems Command

NASA Technical Memorandum 86005 USAAVSCOM Technical Memorandum 84-A-9

An Experimental Investigation of the Parallel Blade-Vortex Interaction

F. X. Caradonna
G. H. Laub
C. Tung, Aeromechanics Laboratory, U. S. Army Research and Technology Laboratories-AVSCOM
Ames Research Center, Moffett Field, California

National Aeronautics and Space Administration
Ames Research Center
Moffett Field, California 94035

United States Army
Aviation Systems
Command
St. Louis, Missouri 63120

AN EXPERIMENTAL INVESTIGATION OF THE PARALLEL BLADE-VORTEX INTERACTION

F. X. Caradonna, G. H. Laub, and C. Tung
Aeromechanics Laboratory, U.S. Army Research and Technology Laboratories (AVSCOM)
NASA Ames Research Center, Moffett Field, California, U.S.A.

ABSTRACT

A scheme for investigating the parallel blade-vortex interaction (BVI) has been designed and tested. The scheme involves setting a vortex generator upstream of a nonlifting rotor so that the vortex interacts with the blade at the forward azimuth. The method has revealed two propagation mechanisms: a "type C" shock propagation from the leading edge induced by the vortex at high tip speeds, and a rapid but continuous pressure pulse associated with the proximity of the vortex to the leading edge. The latter is thought to be the more important source. The effects of Mach number and vortex proximity are discussed.

1. INTRODUCTION

The blade-vortex interaction (BVI) is the subject of some of the most intensive research in fundamental rotor aerodynamics. This interest in the BVI results from the realization that it is a primary source of impulsive noise and that compressibility is an important aspect of the problem (ref. 1). More recently, an extensive review of rotor loads data has pointed out some serious deficiencies in our ability to predict vibratory loading (ref. 2). One possible reason for these failures may lie in our current lack of understanding of the BVI.

References 1 and 2 are especially interesting when considered in terms of the current beginnings of an ability to compute the compressible BVI. To date, computational work has involved a number of finite-difference schemes to simulate the interaction of an ideal or Lamb vortex with an airfoil (refs. 3-5). All these schemes have modeled a two-dimensional flow, which emulates the parallel interaction of a rotor with a vortex (fig. 1). However, this work has been devoid of corroborative data, because there seems to be no simple way to experimentally simulate the two-dimensional, Mach-scaled BVI in the nonrotating environment. Furthermore, the investigation of the parallel BVI on a rotor is complicated by the difficulty of determining the location, strength, and structure of the interacting vortex. This paper presents some early results from a recently tested means to produce parallel BVIs in which the vortex location and strength can be easily measured and controlled.

2. EXPERIMENTAL SETUP

The present approach is a scaled-up version of a setup originally employed by McCormick and Surendraiah (ref. 6). The idea is to study BVIs in a rotary wing environment in which the rotor interacts with but does not generate the vortex in question. The required vortex generation is readily accomplished with a wing mounted upstream of a model rotor.

Such a test was recently performed in the U.S. Army Aeromechanics Laboratory's 7- by 10-Foot Wind Tunnel at Ames Research Center. A semispan wing model was located upstream of the tunnel test section such that the tip vortex that was produced would encounter a model rotor at the $\psi = 180°$ azimuth angle. The wing had an 18-in. chord with a constant NACA 0015 profile. In the process of positioning the wing model, the tip vortex was located by smoke-flow visualization and by measuring the flow field with a hemispherical, five-hole yaw probe which could be traversed vertically, horizontally, or radially around the vortex.

Figure 2 shows ammonium bisulphate smoke being emitted from the wing tip in a test to ascertain the interference effects between the vortex and the direction probe. This wing-positioning phase of the test was performed before the rotor was installed. Thus, the test section was clear enough to allow easy probe traversing. During this phase of the testing, the direction probe was used to find the strength of the vortex for various wing lengths (the wing was equipped with a removable tip), angles of attack, and downstream distances. The vortex strength was found by assuming axial symmetry and then using the measured tangential velocity to determine a circulation. Measurements using the hemispherical yaw probe were made at several transverse planes downstream of the wing. Typical vertical and horizontal pressure traverses extended for a distance of 1 ft from the vortex center. The radial traverse was performed at a radius of 6 in. from the core center.

Figure 3(a) shows a typical result from the rotary traverse used to check axial symmetry. The flow angle (as indicated by a differential pressure) is seen to be independent of probe location except for a region in the upper left quadrant which is probably the wing vortex sheet (shown in the inset sketch). This region is seen as an unusual pressure deviation on the left portion of the horizontal traverse (shown in fig. 3(b)). In the vertical traverse this deviation does not appear. Therefore, the lower region of the vortex (that is, the region the blade will encounter) is fairly axisymmetric and seems quite representative of what can be computationally modeled. The vortex is also probably typical in structure (if not in size) of the vortex the model rotor would generate. The viscous core region of the vortex is about 2 in. in diameter. The outer rotational region of the vortex could be as much as 10 times greater; however, this has not been determined as yet. At present, only the strength of the vortex has been measured. For incidence angles of 11° and 6°, the nondimensional circulations, $\Gamma_V/U_T C_W$ (where Γ_V is the vortex circulation, U_T the tunnel speed, and C_W the chord of the wing), were found to be 0.46 ±0.2 and 0.22 ±0.01, respectively. These particular values were determined at the downstream location that the rotor tip would occupy at $\psi = 180°$. The circulation was not found to vary significantly over the range of streamwise locations or wing lengths tested.

Following the above vortex measurements, the rotor was installed. This model was a two-bladed teetering-rotor system equipped with full collective and cyclic control. The blades were 7 ft in diameter and 6 in. in chord with an untapered, untwisted NACA 0012 profile. These blades were constructed almost entirely of balsa and carbon/epoxy composites and were quite stiff (first flap and torsional

frequencies were 30 Hz and 290 Hz, respectively) in order to minimize blade motion effects. The blades were equipped with 12 absolute pressure transducers (Kulite model XCQ-63-903-25A), all located on the same blade side. However, both upper- and lower-surface pressures were obtained by reversing the direction of rotation of the rotor. This procedure involved only the disconnection and reconnection of the blade-retention straps and pitch links and the reversal of the vortex-generator incidence.

Figure 4 shows the rotor installed with the vortex generator mounted upstream. The distance from the wing trailing edge to the rotor tip (at $\psi = 180°$) was 48 in. The wing was mounted from the tunnel ceiling to minimize the possibility of the rotor encountering the wing vorticity sheet. The wing length was chosen so the vortex would pass over the top of the rotor, thus minimizing hub interference effects. The rotor was always operated at zero collective angle in order to minimize any distortion of the vortex. Likewise, the cyclic controls were always adjusted to minimize flapping. Thus, the distance from the blade to the vortex was well controlled. This blade/vortex distance was measured by taking simultaneous upper and side view photographs, as well as stroboscopic video recordings of the smoke-visualized vortex core. Figure 5 shows simultaneous upper and side view photographs of a BVI, for a tip Mach number of 0.5 and an advance ratio, μ, of 0.2.

The pressure data were recorded on analog tape and later digitized. In the analysis process it was necessary to ensemble-average the data in order to remove random flow effects and electrical noise. Since the flow event being studied is a very brief one, it is vital to verify that it is sufficiently repeatable to avoid being lost in the averaging process. It was determined that the BVI event is unaffected by the averaging process. The only problem discovered to date involve measurements of shock motion under marginally supercritical conditions. These shock motions do not always repeat and are partially rounded by the averaging process. The typical data treatment consists of an average of 64 data samples (each sample consists of 12 channels of 2048 data points per revolution) acquired over a 15-sec period.

3. RESULTS

Data were acquired for a range of tip Mach numbers M_T ranging from 0.3 to 0.8. A wide range of advance ratios was also tested; however, for the high M_T runs we were limited to about $\mu = 0.2$ by the vibratory loads. Therefore, the data at the greatest tip speed cover high transonic flows for the advancing blade and the low transonic regime at $\psi = 180°$ where the BVI occurs.

All cases shown in this paper are for runs in which the vortex generator was set at 11° incidence. Following recent computational practice, the strength of the vortex is expressed as the lift, C_{L_V}, which the blade section would have (at its local rotational speed) in order to have the same circulation as the vortex. The results to be shown are for a fixed value of C_{L_V}. This implies that the advance

ratio is also fixed. Therefore, the only variables to be discussed are tip Mach number, M_T, and the normal distance, Y_v, from the blade to the vortex at the closest approach.

The subcritical cases all bear a strong resemblance to each other. Figure 6 shows the azimuthal pressure histories for a number of upper and lower surface transducers. (Recall that the blade is only instrumented on one side and that upper and lower pressures are obtained by reversing the blade and vortex directions. The real orientation to keep in mind is whether the transducers are on the vortex side of the blade or on the opposite side. However, most readers equate BVIs with the underside of an operational blade. Therefore, in all future references we shall ignore the actual test orientations and equate the terms, "vortex side," and "lower surface.") The tip Mach number M_T in figure 6 is 0.6 and the advance ratio μ is 0.2. Therefore, the local Mach number M_L at this radial station (0.893R) is 0.536 at $\psi = 180°$. The closest blade/vortex distance is $Y_v/c_A = 0.4$ and the strength of the vortex is $C_{L_v} = 0.62$. By far, the most prominent effect of the near blade/vortex encounter at $\psi = 180°$ is the sharp pressure perturbation in the leading-edge region. (A BVI of the conventional kind is also seen near $\psi = 78°$.) On the vortex side of the blade, this perturbation is seen as an increasing expansion as the blade approaches the vortex, followed by a rapid compression or increase in pressure level which occurs when the vortex and leading edge are near each other. On the reverse side of the blade, the pressure perturbation is the opposite of what occurs on the vortex side. That is, the pressure increases as the vortex approaches and then undergoes a rapid expansion. These effects are also seen in all the other transducers, but the magnitude of the effect decreases rapidly with increasing distance from the leading edge. The overall shape of the perturbation also changes with distance from the leading edge. As the trailing edge is approached, the perturbation becomes a compression pulse (rather than a pressure-level increase) on the vortex side and an expansion pulse on the opposite side. Another interesting feature of these signals is that insofar as can be measured on this scale they all seem to occur simultaneously. It is now necessary to examine the BVI on the scale of a chord-transit interval.

Figure 7 shows an entire chordwise set of pressure variations on the vortex side of the blade. With the aid of the video flow visualization we have rescaled time by chord passages rather than by azimuth angle. The figure shows the pressure variations over the time that the vortex traverses from 0.5c upstream of the leading edge to 1.0c downstream of the trailing edge. For this case the local Mach number M_L is 0.624 ($M_T = 0.7$) and the vortex distance is only 0.22c from the rotor-blade centerline. Again, we see that the central event is a steep pressure rise which begins when the vortex is at the leading edge. This pressure jump is seen to occur in two phases—an initial steep phase followed by a more gradual phase. (For weaker BVIs, the transition into the second phase is not necessarily so sharp.) The time interval of the initial steep pressure rise is about 0.25c. The pressure rise at the first transducer ($x/c = 0.02$) occurs about 0.19c (in time) ahead of the rise in the second transducer ($x/c = 0.11$). Therefore, the initial passage time of the pressure rise seems slower than the passage time of the vortex itself at the leading edge.

However, the pressure rise for the third ($x/c = 0.20$) and all subsequent transducers is nearly simultaneous. A probable explanation of this near simultaneity is that the vortex-induced pressure rise at the leading-edge region is being propagated downstream. Even at this relatively high speed, the downstream propagation rate (that is, the local Mach number plus one) is 2.6 times greater than the local Mach number. This rate is greater than what can be accurately measured with the present pressure data. In figure 7, this family of disturbances has, therefore, been labeled a "propagated" disturbance.

The total picture is complicated at $x/c = 0.31$ by the appearance of another pressure rise with a different phasing from the previously discussed signals. This disturbance may be a local flow separation, because it occurs in a region of adverse pressure gradient. Furthermore, this disturbance is convecting downstream at about one-half of the free-stream speed. Such a slow convection suggests the existence of a separation region. However, the disturbance is not so severe as to cause a drastic flow breakdown. At no place in this picture is there any trace of a disturbance moving at the free-stream speed. In other words, after the initial leading-edge event, there is nothing in the pressure data that clearly reveals the presence of the vortex. However, all the smoke-visualizations show what appears to be a well-structured vortex passing very close to the blade surface.

Figure 8 shows the upper-surface pressure variations corresponding to those in figure 7. The "propagated" signal is very clearly seen in the figure, and it has the opposite sign of that on the lower surface. It is not clear if there is a convected disturbance to be seen here. As mentioned previously, the above description is typical of almost all the subcritical cases that were run. Figure 9 shows a set of lower-surface pressure variations for a low-speed ($M_L = 0.268$) and much weaker ($Y_v/c = 0.5$) BVI. The variations from the previous case are not great. The pressure rise seems more concentrated at the leading edge, and the propagated disturbance is much weaker. Figures 10 and 11 show the lower- and upper-surface pressure variations (in nondimensional form) for $M = 0.536$ and $Y_v/c = 0.40$. Figure 12 shows chordwise pressure distributions corresponding to the four marked times in the previous two figures. These figures show the rapid shift from a negative to a positive lift. During the time that the vortex-induced pressure pulse occurs, the aft upper and lower pressures are not approaching each other, and it is not clear that the Kutta condition will take a classical form.

Before discussing some of the BVI data at supercritical conditions, it is helpful to first consider some of the high-speed runs in which the vortex was absent. Figure 13 shows a number of pressure traces from the second rotor quadrant of such a case. The combination of high tip Mach number ($M_T = 0.7$) and advance ratio ($\mu = 0.3$) produces a strong shock. In the second quadrant, the local Mach number is decreasing, and the shock is weakening as it advances on the leading edge. It is especially interesting that the shock—although greatly weakened by this time—seems also to pass the forward transducer ($x/c = 0.02$). Actually, the shock is not always as weak as appears, because this figure is an average. A check of some individual records reveals that the shock appearance at the leading edge is intermittent.

This then appears to be another example of the "type C" shock propagation from the leading edge, first described by Tijdeman (ref. 7).

The highest speed runs performed were for a tip speed of $M_T = 0.8$ and an advance ratio of 0.2. When the vortex generator was inoperative, type C shock motion was not observed. When a vortex was present, leading-edge shock propagation did occur. Figure 14(a) shows the behavior of several pressure traces in the vortex-passage region. Pressure traces Nos. 2 and 3 are widely separated from the others, because they alone are in a supercritical flow region. Furthermore, they appear to remain supercritical for most of the time that the blade is in transit over the vortex. The flow is generally decelerating, however, and the shock moves forward past transducer No. 3 just as the vortex passes the trailing edge. We then can trace the motion of the shock until it passes the first transuducer at $X_V/c \cong 1.8$. Such vortex-induced shock propagation was first predicted by George and Chang (ref. 4).

Figure 14(b) shows a series of chordwise pressure distributions corresponding to the vortex locations marked at the bottom of figure 14(b). What stands out in these distributions is that the negative lift induced by the vortex does not change sign until after the vortex has left the trailing edge, whereas at lower speed (fig. 12) the lift reversed much sooner. The spatial resolution is not sufficient alone to show the later shock motion. However, the time data have been used to imply in these figures what the spatial appearance of the forward propagating shock must be. In summary, the supercritical cases show two propagation phenomena: the type C and the vortex-induced pressure pulse. Of the two phenomena, the latter has the greater magnitude and may be the more significant event.

In order to summarize all the data, it is useful to compare a number of leading-edge transducer outputs for a range of Mach numbers. Figure 15 shows a number of lower-surface (that is, the vortex-side) pressure signals from the first chordwise transducer. The only variable in the figure is M_L ($Y_V/c = 0.4$, $C_{L_V} = 0.62$). The similarity of all the pressure variations is fairly impressive. In general, the magnitude of the steepest portion of the pressure rise is seen to decrease with increasing Mach number. The highest speed curve is on a higher overall pressure level consistent with its supercritical pressure distribution. However, its pressure variation is similar to all the others. To get some idea of the spatial distribution of the pressure rise, we have defined a pressure rise for the steep portion of the pressure variation (shown in the inset of fig. 16). Choosing a pressure jump magnitude is a rather subjective and imprecise process. However, the point here is not so much accuracy as it is a general grasp of the spatial distribution. What emerges in figure 16 is an impression that the effect of increasing Mach number is to broaden the spatial extent of the pressure jump. The supercritical case is rather different in that it manifests in a rapid drop, which reflects the presence of the shock. The pressure rise on the upper surface is also plotted spatially in figure 17. Here we see also a decreasing magnitude with increasing Mach number. However, the subcritical curves are much more similar in character to each other and look quite similar to a linear lift distribution. Again, the high-speed case has a very different character.

Finally, the effect of blade/vortex proximity to the blade is shown in figure 18. The first chordwise transducer output is presented for three different vortex distances. Notice that the increments in vortex distance are not equal. However, the actual changes in the vortex-generator length were in equal 1-in. increments. This demonstrates that the blade-induction effects on the vortex are increasing very rapidly as distance decreases. It comes as no surprise that the close-interaction case has much the greatest pressure rise. However, the qualitative nature of the pressure rise is similar for all three cases.

4. CONCLUDING REMARKS

A pilot test has been conducted of a scheme for studying the parallel BVI. The method permits good control over the vortex, whose position can be easily determined by smoke visualization; it also permits a close approach to full-scale Mach and Reynolds numbers. Blade-vortex encounters have been recorded with pressure transducers for a range of local Mach numbers varying from near incompressible flow to the low transonic. The results presented here are but a small sample of the data that have been acquired. These and other results show that there are two scales over which events occur. The first and obvious effect is that the lift decreases and subsequently increases, a result of the effective varying angle of attack of the blade induced by the vortex. The time-scale of this event is measured in chords, say, 10. The second time-scale is much shorter.

The primary event measured in this study was a brief pressure pulse, the steepest portion of which is about 0.25c in duration and which begins when the vortex is at the leading edge. This vortex-induced pulse is primarily a compression on the vortex or underside of the blade and an expansion on the other side. By far the greatest effect is on the forward 20% of the blade; however, it is detectable along the entire chord. Moreover, the chordwise phase delay of this pulse is smaller than can be accurately measured for the latter 80% of the chord. A probable interpretation of this event is that we are seeing the propagation rearward of a signal emanating from the leading edge. Presumably, the signal is propagating in all directions as well. If this supposition is correct, this may be the source of vortex-induced blade slap. Previous studies have associated this blade slap with compressibility effects. Strangely enough, we find that the non-dimensional magnitude of the vortex-induced pulse decreases with increasing Mach number.

Finally, although the vortex-induced pressure variations are steep, we have never found them to be discontinuous. We have found a second propagation mechanism at high speed: type C shock propagation. However, this is a transonic, low-frequency phenomenon associated with the angle-of-attack variation rather than the closeness of the vortex. The importance of vortex-induced type C propagation as an acoustic source is unknown. However, directivity considerations may point to a relative unimportance of this mechanism. "Type C" motion propagates in the chordwise direction and current indications are that BVIs cause a primarily downward directed propagation.

It comes as no surprise that we have produced more questions than answers. However, it is clear that our scheme for investigating the BVI is a workable one which can provide much needed insight into the problem. In future tests, the effects of vortex size will be investigated and the flow off the blade surface will be studied. Perhaps most important of all, this particular test configuration is a readily computable one. Efforts to duplicate these data computationally will provide an important stepping stone to a yet distant goal of computationally simulating an entire rotor flow-field.

REFERENCES

1. Boxwell, D. A.; and Schmitz, F. H.: Full-Scale Measurements of Blade-Vortex Interaction Noise. Presented at the 36th Annual National Forum of the American Helicopter Society, Washington, D.C., May 1980.

2. Hooper, W. E.: The Vibratory Airloading of Helicopter Rotors. Presented at the 9th European Rotorcraft Forum, Stresa, Italy, Sept. 1983.

3. Caradonna, F. X.; Desopper, A.; and Tung, C.: Finite Difference Modeling of Rotor Flows Including Wake Effects. Presented at the 8th European Rotorcraft Forum, Aix-en-Provence, France, Aug. 1982.

4. George, A. R.; and Chang, S. B.: Noise due to Transonic Blade-Vortex Interactions. Paper No. A-83-39-50-D0000, 39th Annual National Forum of the American Helicopcer Society, May 1983.

5. McCroskey, W. J.; and Goorjian, P. M.: Interactions of Airfoils with Gusts and Concentrated Vortices in Unsteady Transonic Flow. AIAA Paper 83-1691, July 1983.

6. McCormick, B. W., Jr.; and Surendraiah, M.: A Study of Rotor Blade-Vortex Interaction. Presented at the 26th Annual National Forum of the American Helicopter Society, Washington, D.C., June 1970.

7. Tijdeman, H.: Transonic Flow past Oscillating Airfoils. Ann. Rev. Fluid Mech., vol. 12, 1980, pp. 181-222.

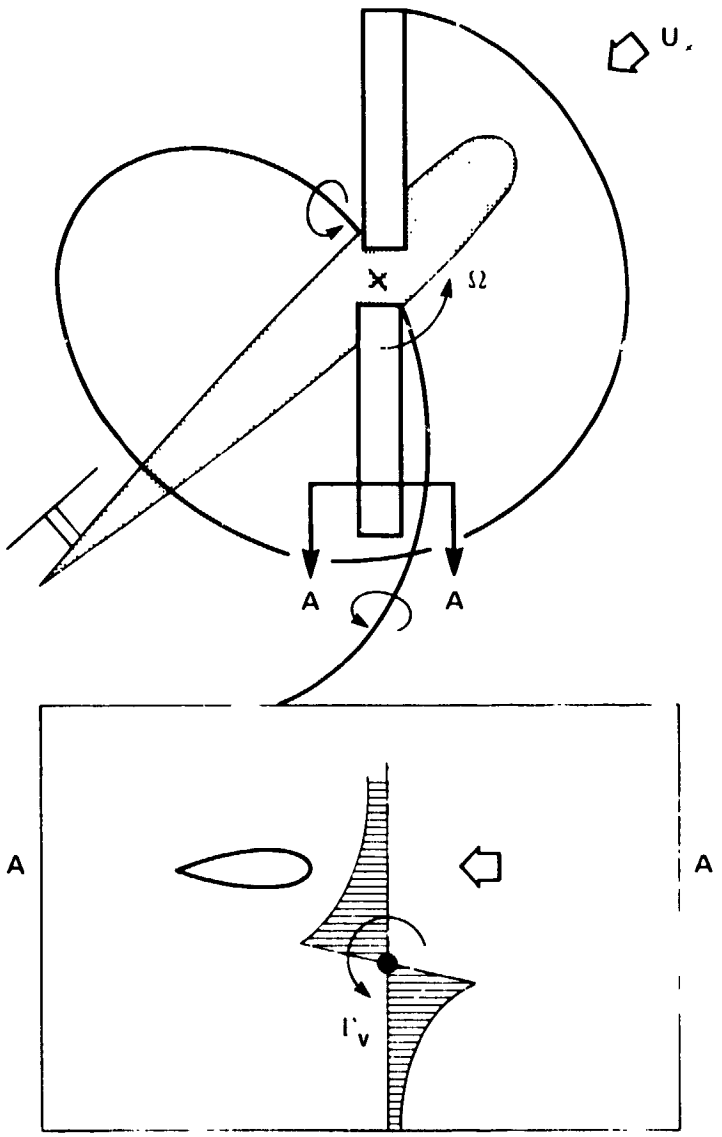

Figure 1. Parallel blade vortex encounter.

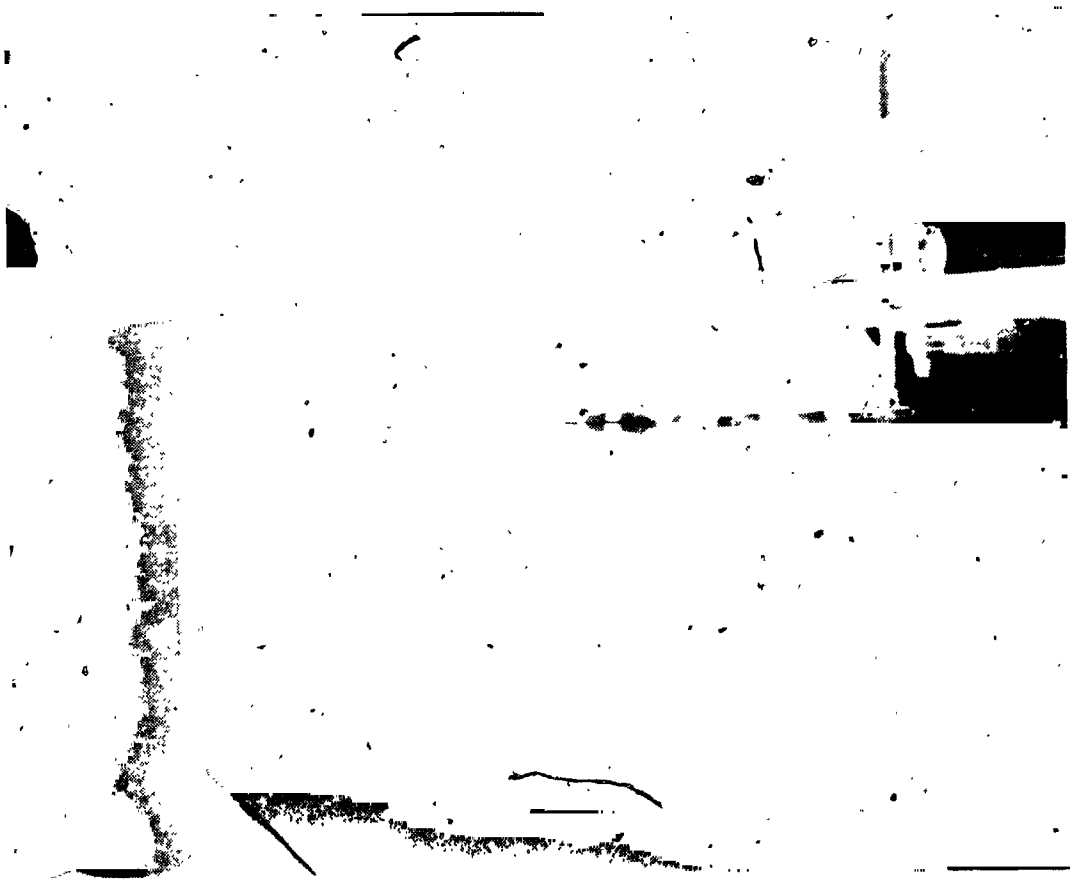

Figure 2. Smoke flow visualization of the tip vortex.

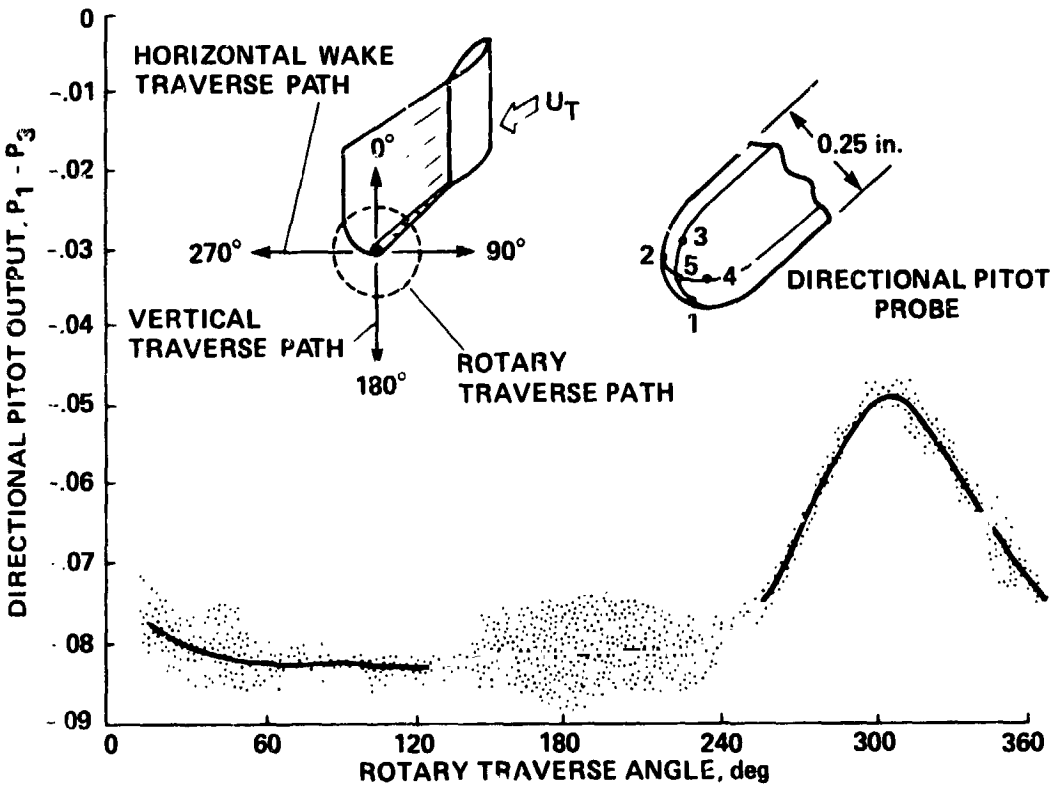

Figure 3(a). Directional pitot probe studies of the tip vortex.

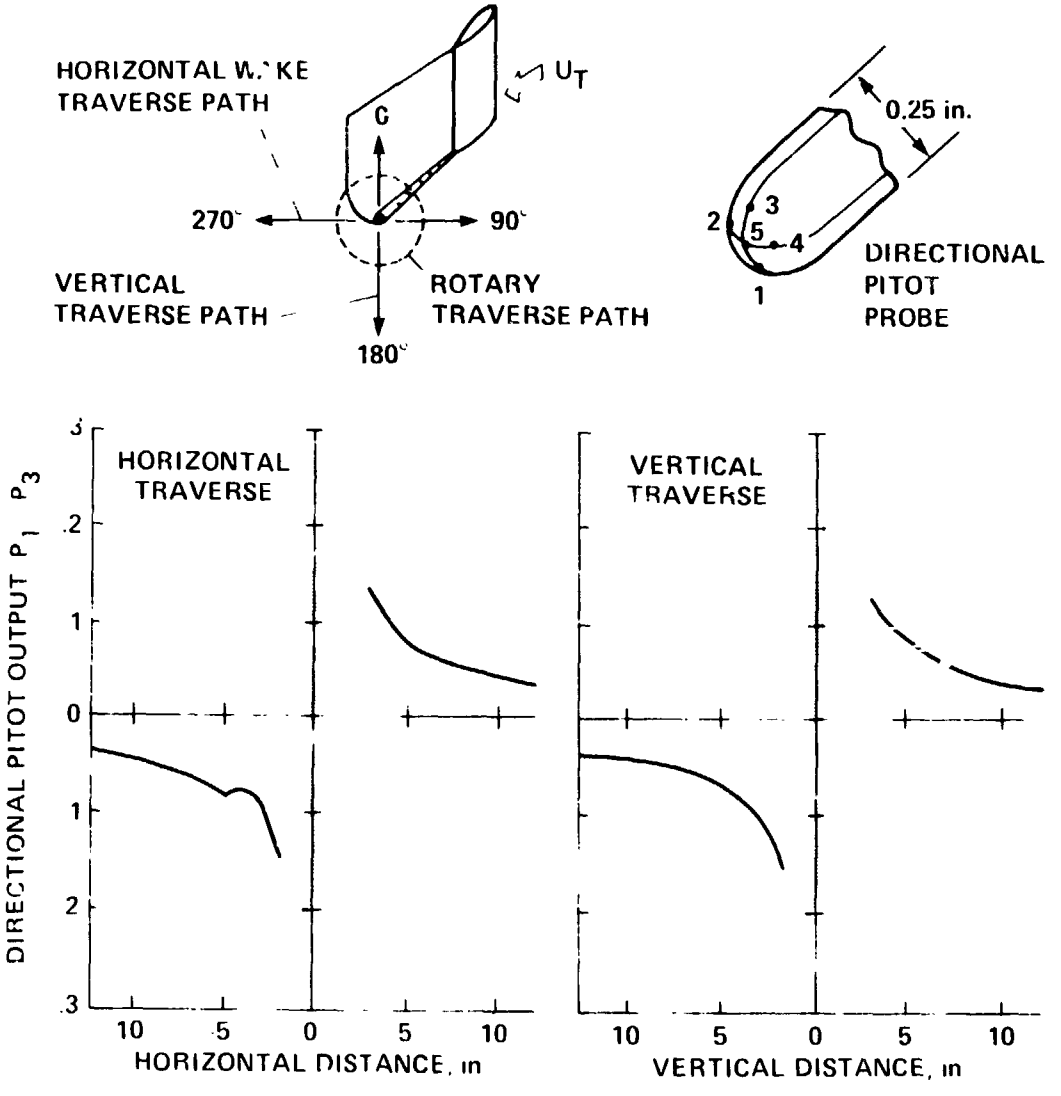

Figure 3(b). Directional pitot probe studies of the tip vortex.

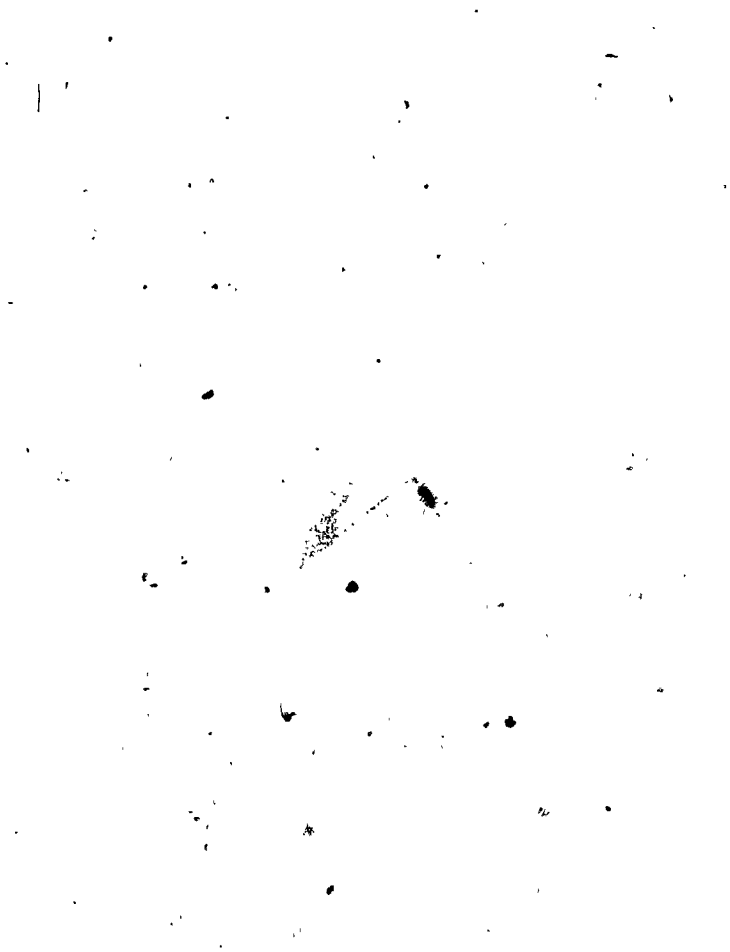

Figure 4. Rotor installation downstream of the vortex generator.

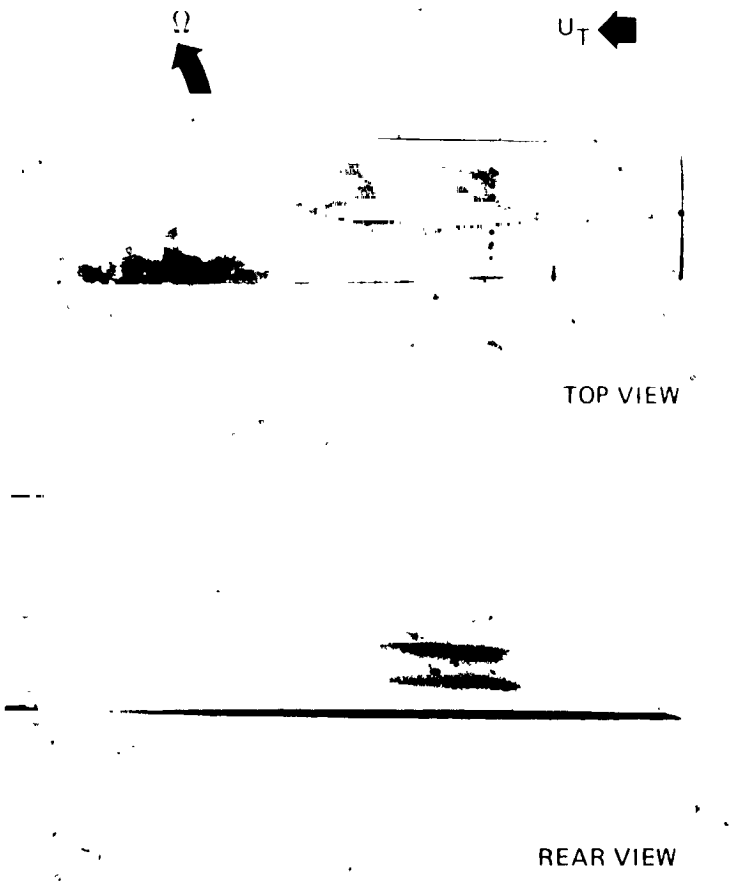

Figure 5. Smoke visualization of a blade/vortex encounter: tip Mach No. = 0.5, advance ratio = 0.2.

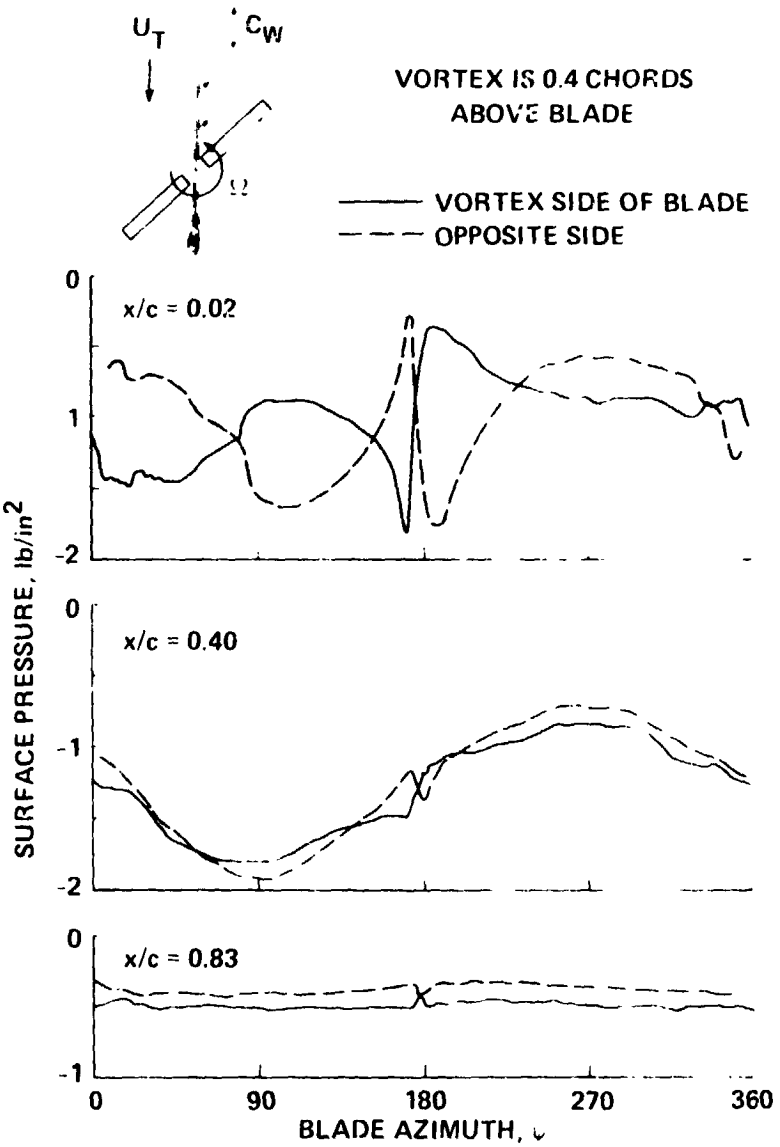

Figure 6. Pressure variations on a rotor interacting with a vortex: $M_T = 0.6$, $U_T/\Omega R = 0.2$, $r/R = 0.893$, $\Gamma_V/U_T C_W = 0.62$.

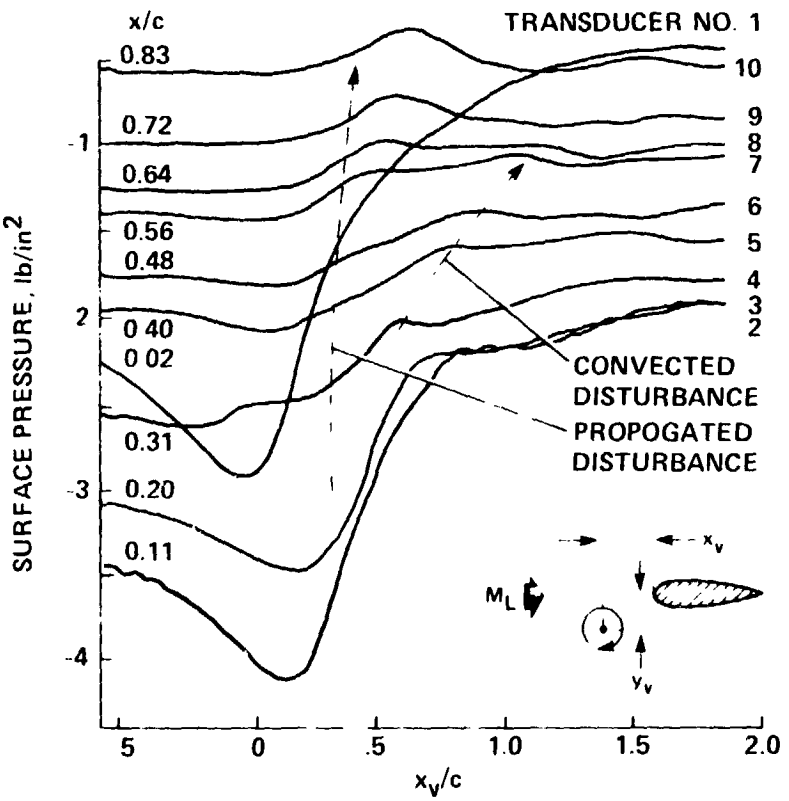

Figure 7. Vortex induced surface pressure variations: M_L = 0.624, C_{LV} = 0.62, y_v/c = 0.22, NACA 0012, lower surface.

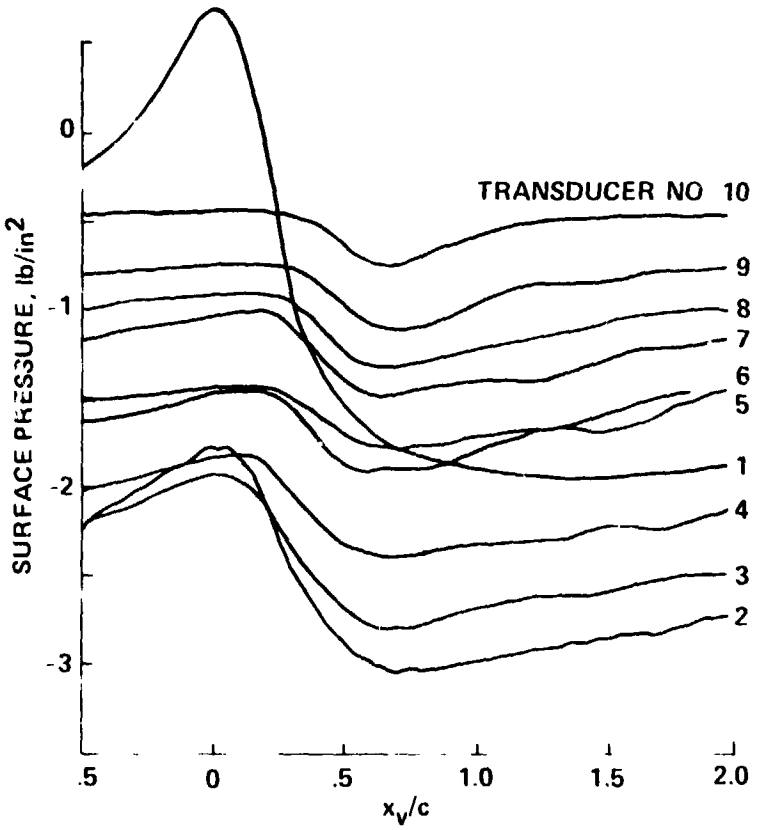

Figure 8. Vortex induced surface pressure variations: M_L = 0.624, C_{LV} = 0.62, y_v/c = 0.22, NACA 0012, upper surface.

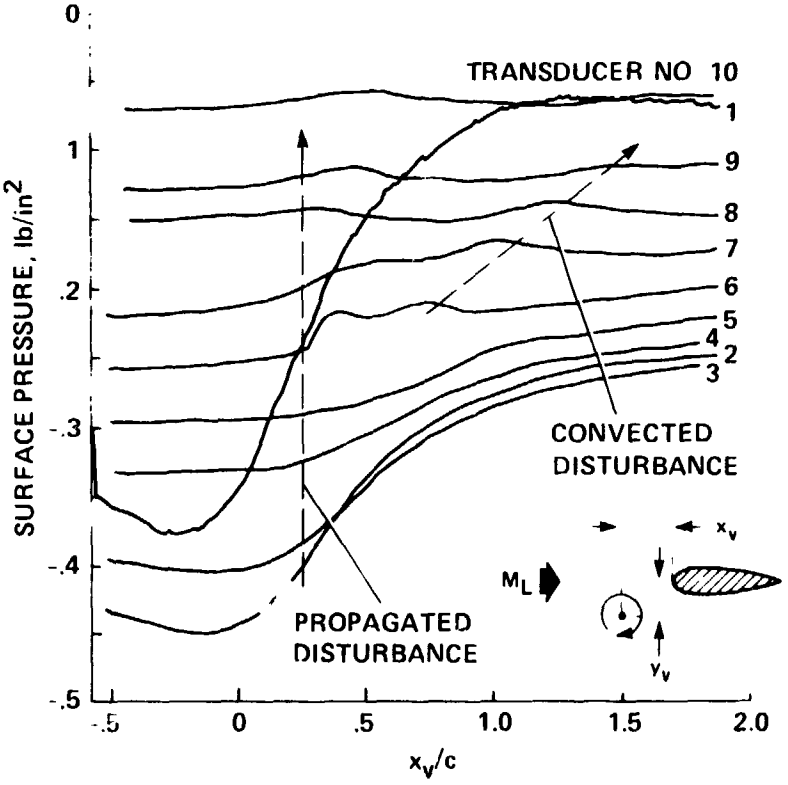

Figure 9. Vortex induced surface pressure variations: M_L = 0.268, C_{LV} = 0.62, y_v/c = 0.5, NACA 0012, lower surface.

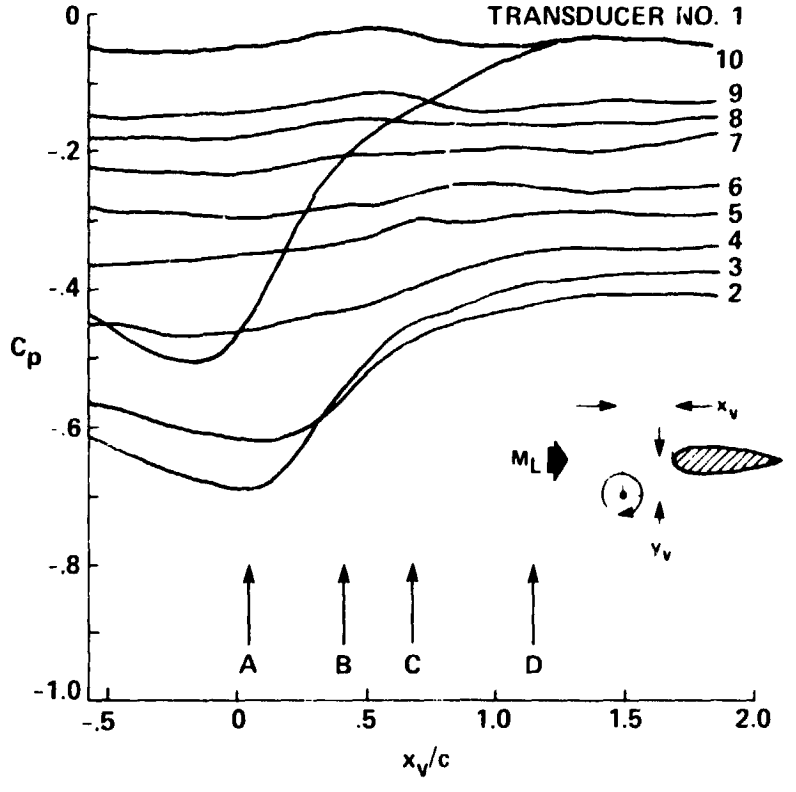

Figure 10. Vortex induced surface pressure variations: M_L = 0.536, C_{LV} = 0.62, y_v/c = 0.40, NACA 0012, lower surface.

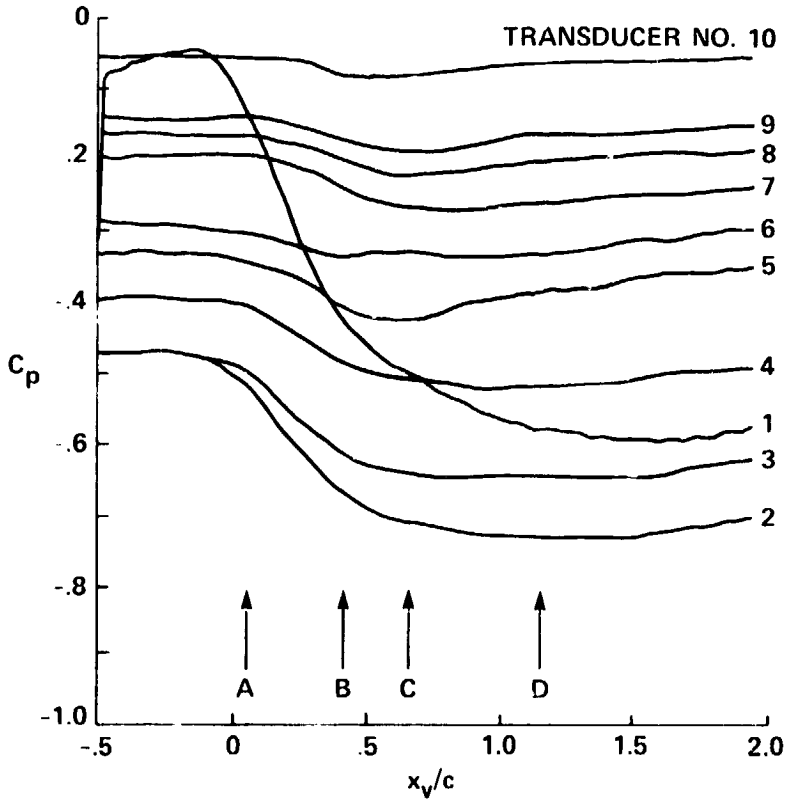

Figure 11. Vortex induced surface pressure variations: M_L = 0.536, C_{LV} = 0.62, y_v/c = 0.40, NACA 0012, upper surface.

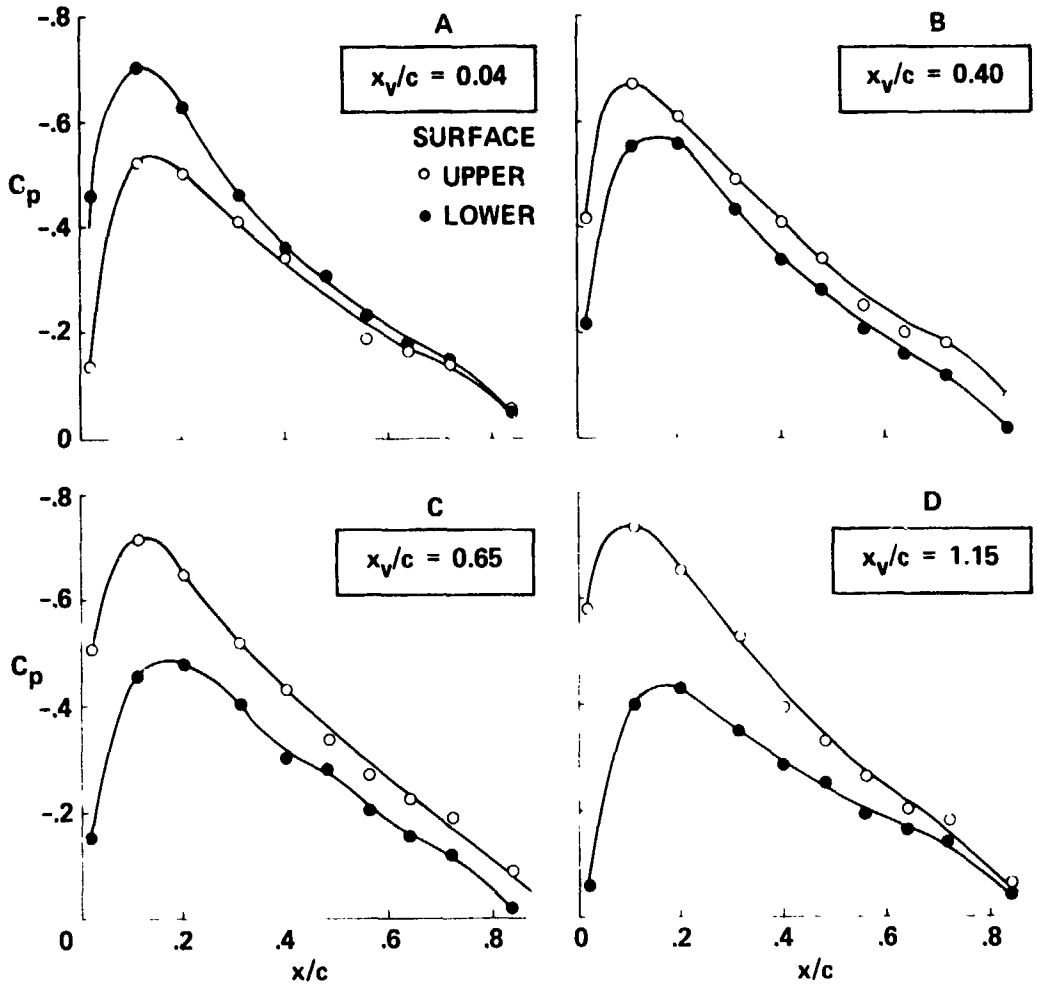

Figure 12. Chordwise pressure distribution as a function of vortex position: M_L = 0.536, C_{LV} = 0.62, y_v/c = 0.40.

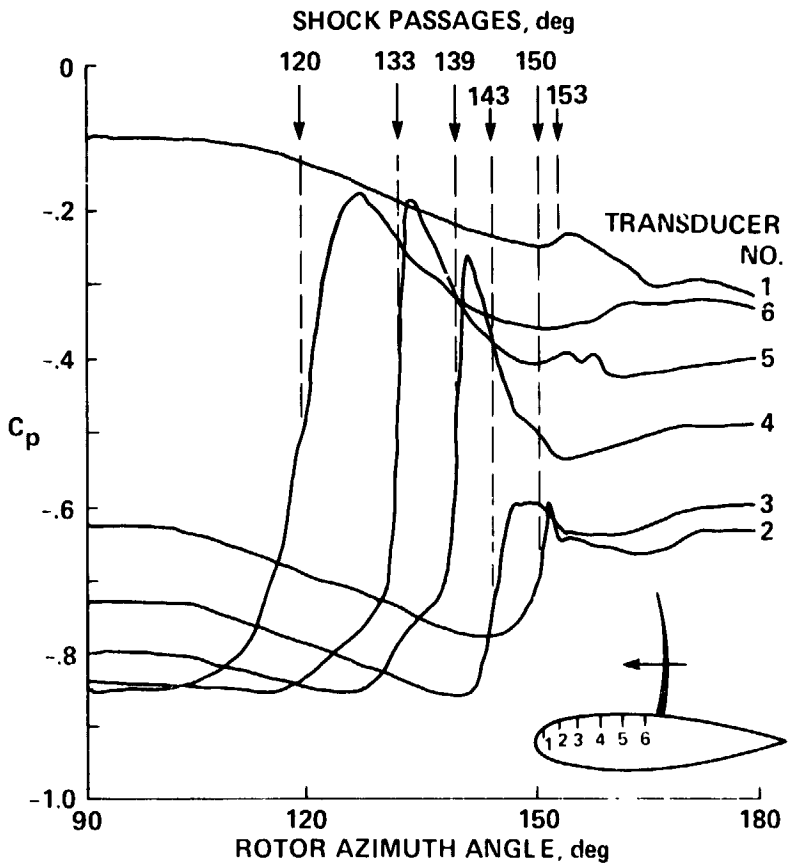

Figure 13. Shock motion on an advancing rotor: no vortex, M_T = 0.7, advance ratio = 0.3, r/R = 0.893, NACA 0012.

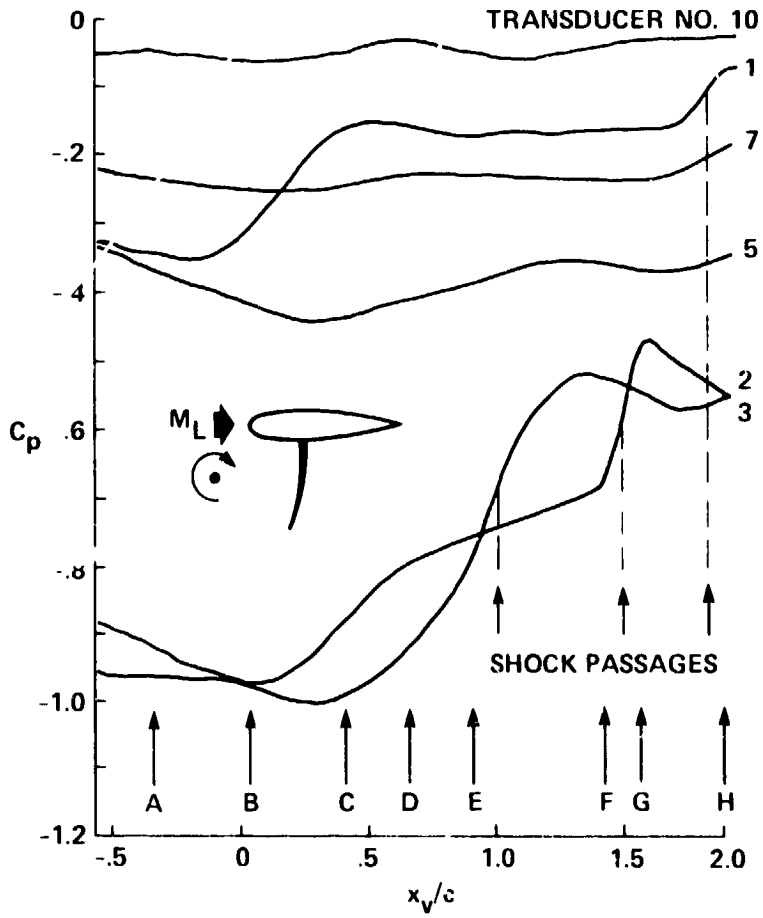

Figure 14(a). Vortex induced surface pressure variations: $M_L = 0.714$, $C_{LV} = 0.62$, $y_v/c = 0.40$, lower surface.

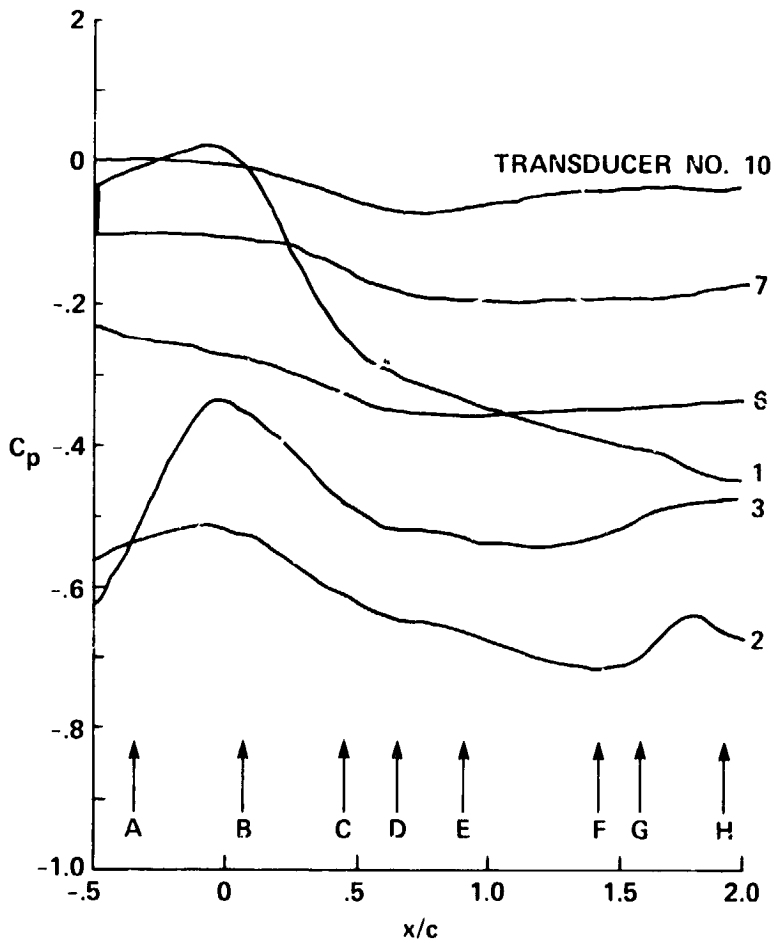

Figure 14(b). Vortex induced surface pressure variations: $M_L = 0.714$, $C_{LV} = 0.62$, $y_v/c = 0.40$, upper surface.

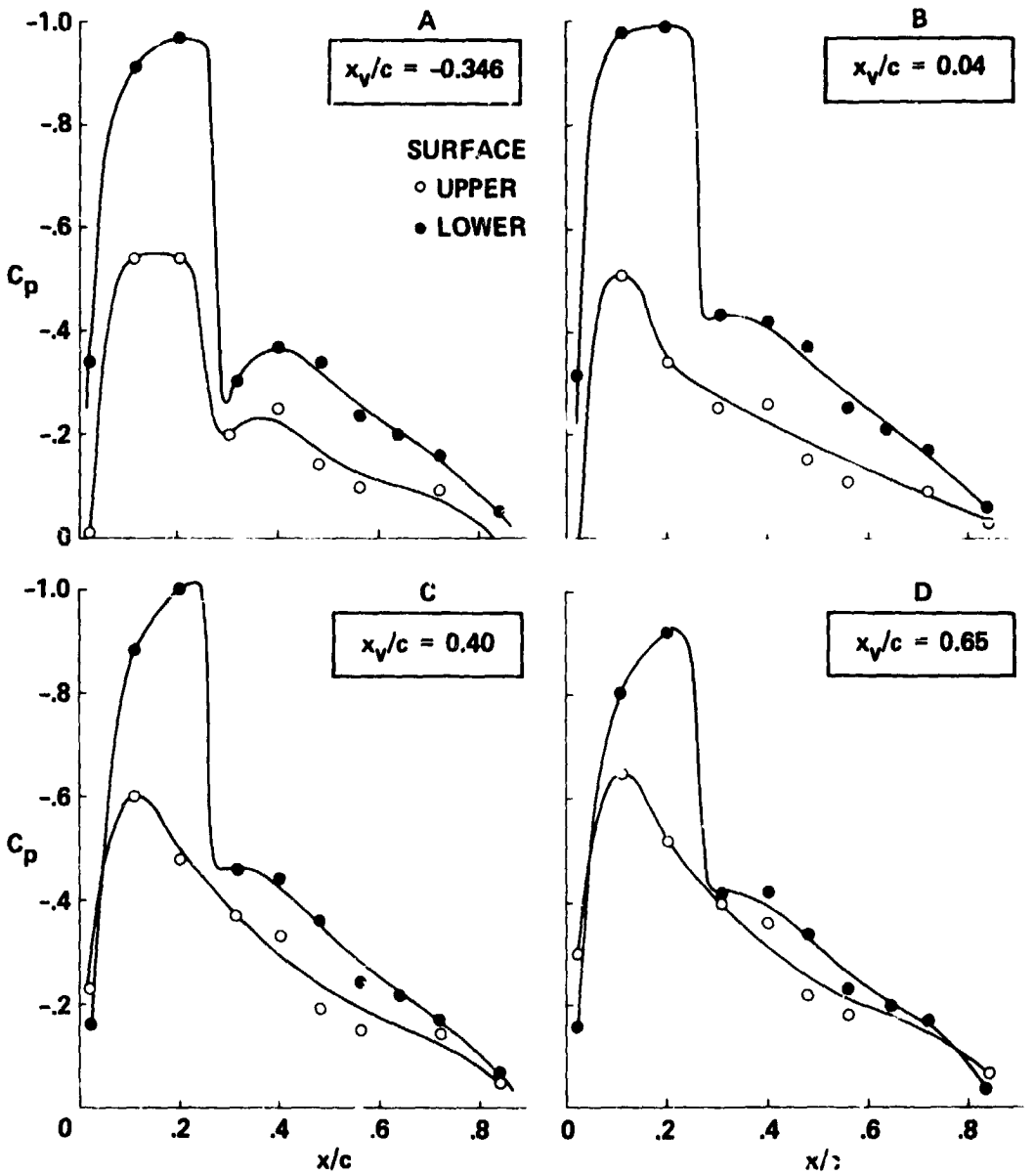

Figure 14(c). Chordwise pressure distribution as a function of vortex position: M_L = 0.714, C_{LV} = 0.62, y_v/c = 0.40.

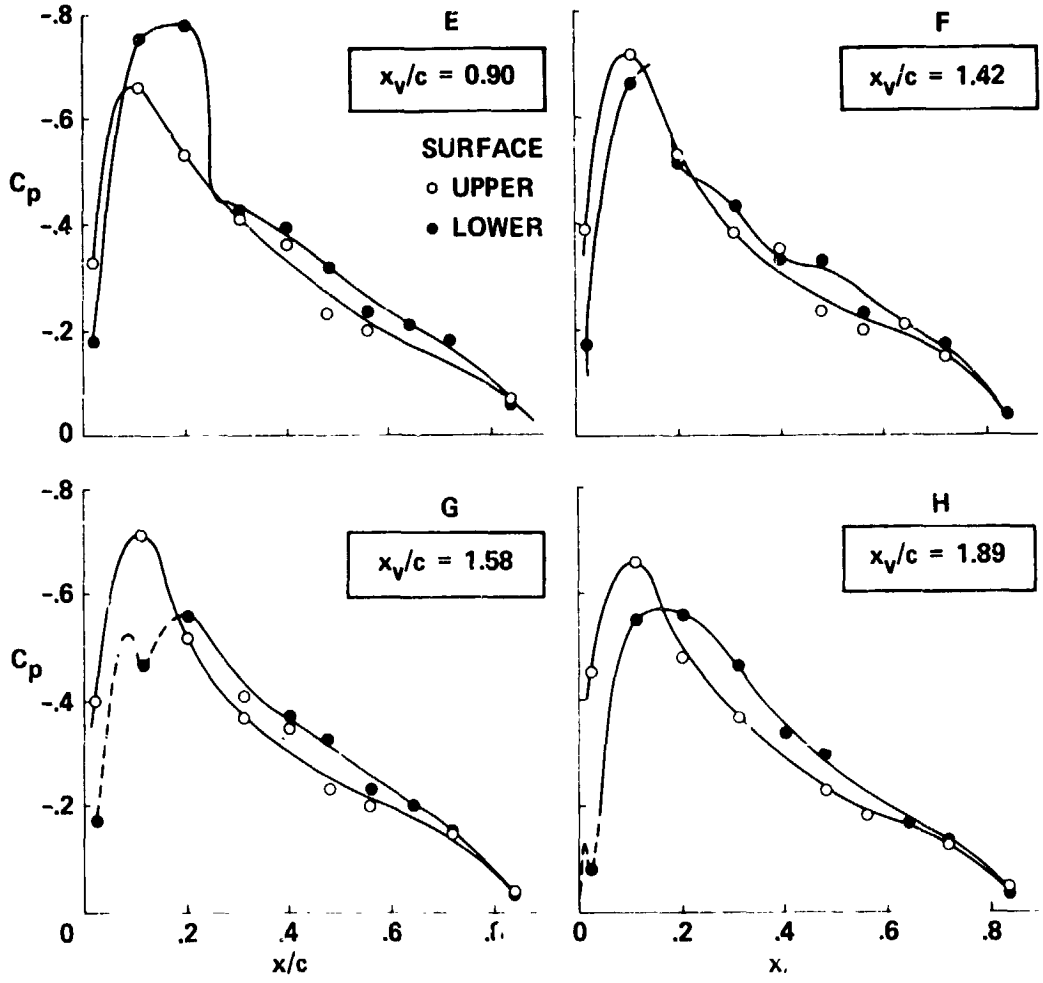

Figure 14(d). Chordwise pressure distribution as a function of vortex position: M_L = 0.714, C_{LV} = 0.62, y_v/c = 0.40.

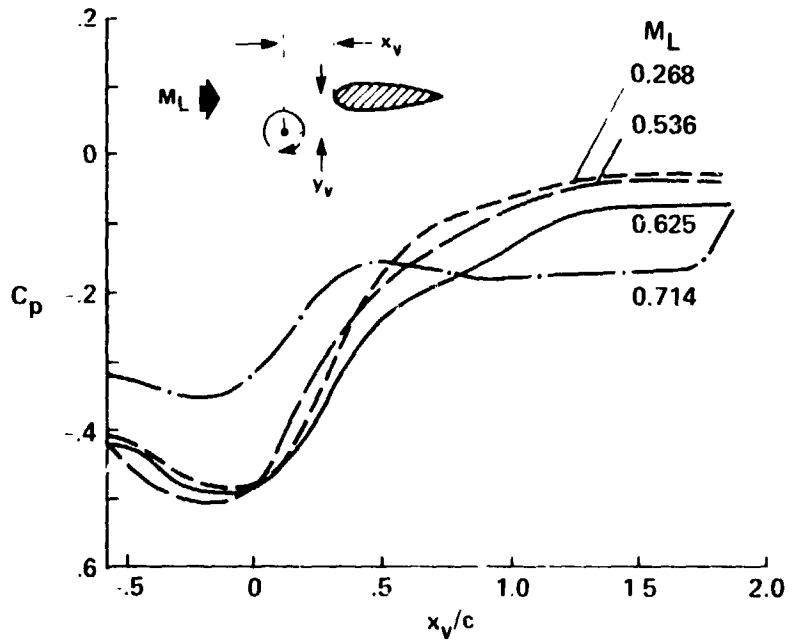

Figure 15. Time histories of the vortex induced pressure rise - lower surface: C_{LV} = 0.62, x/c = 0.02, y_v/c = 0.40, NACA 0012.

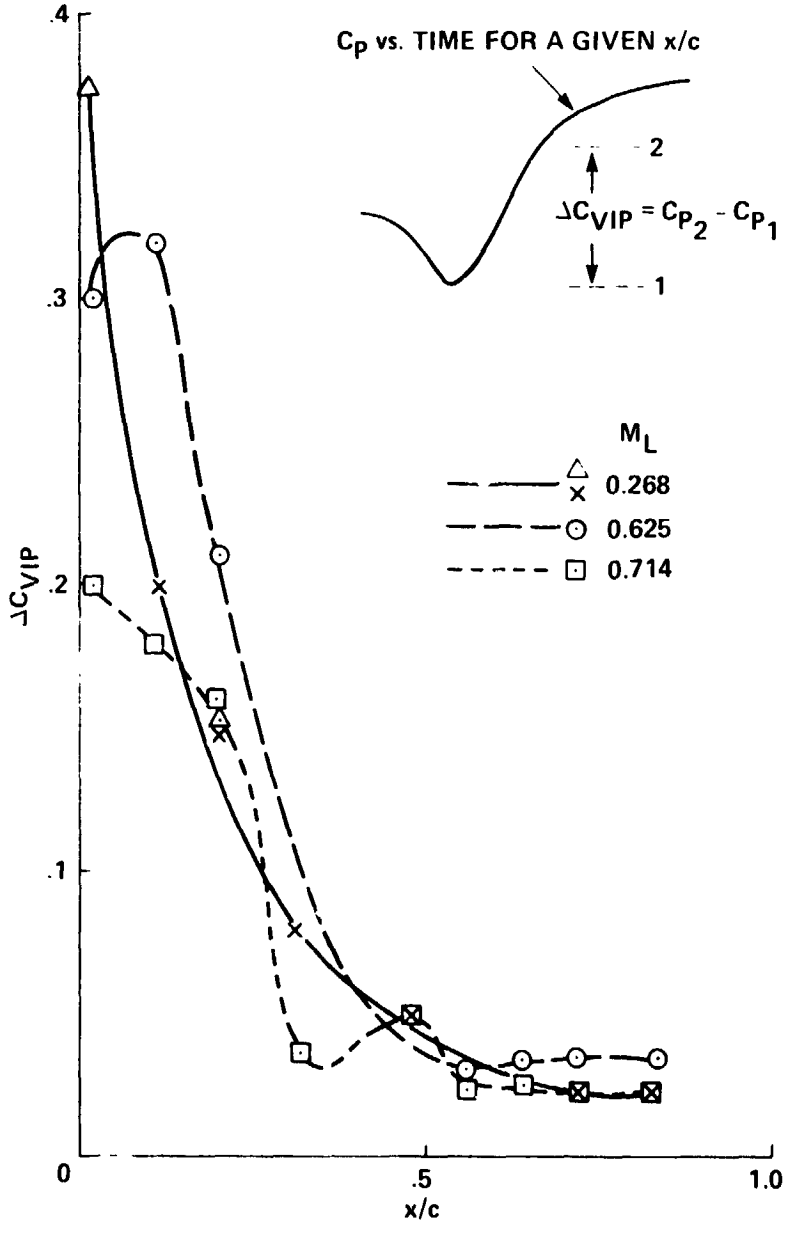

Figure 16. Chordwise distribution of the vortex induced pressure rise lower surface: $C_{LV} = 0.62$, $y_v/c = 0.40$.

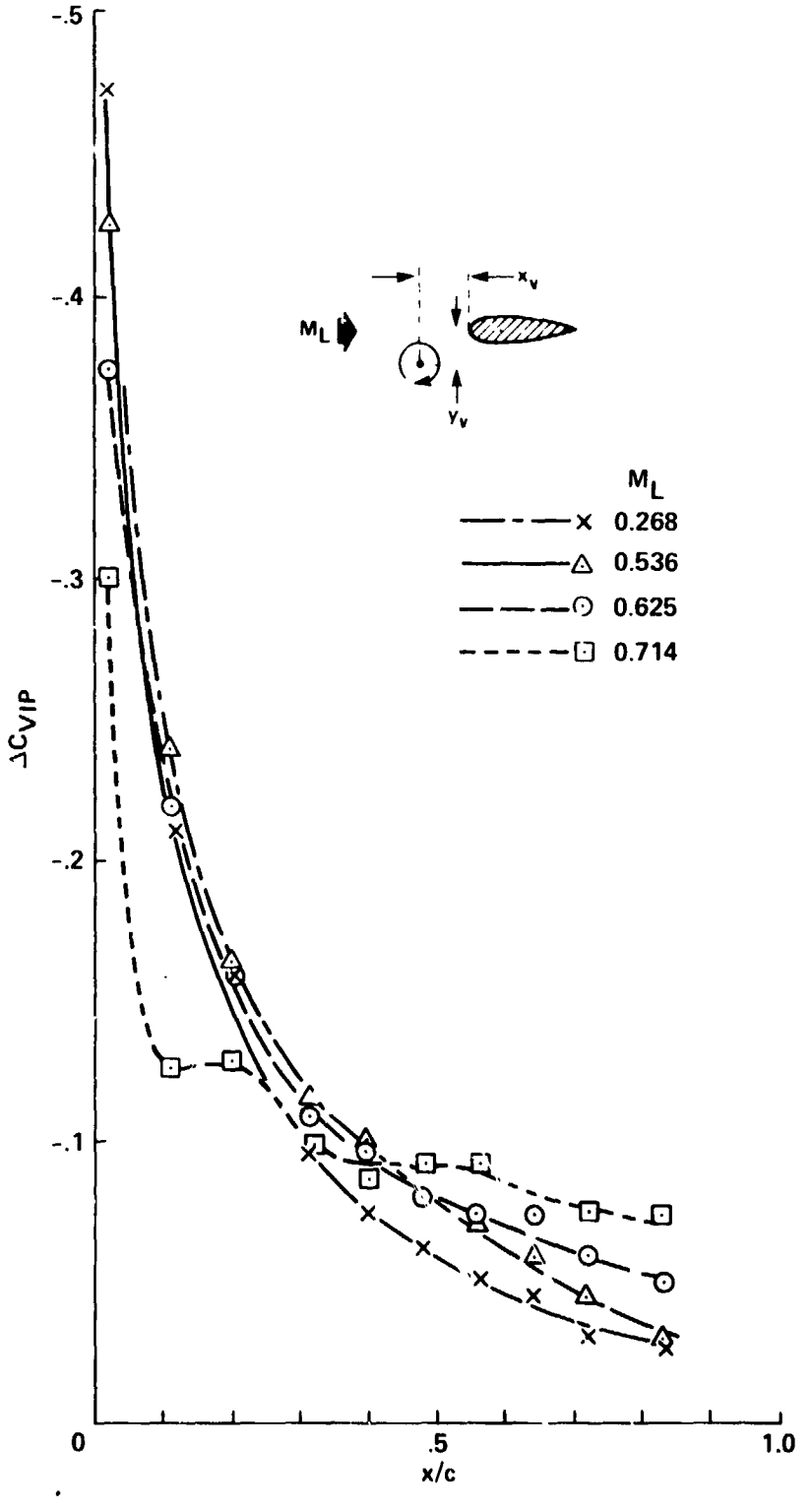

Figure 17. Chordwise distribution of the upper surface pressure drop: $C_{LV} = 0.62$, $y_v/c = 0.40$.

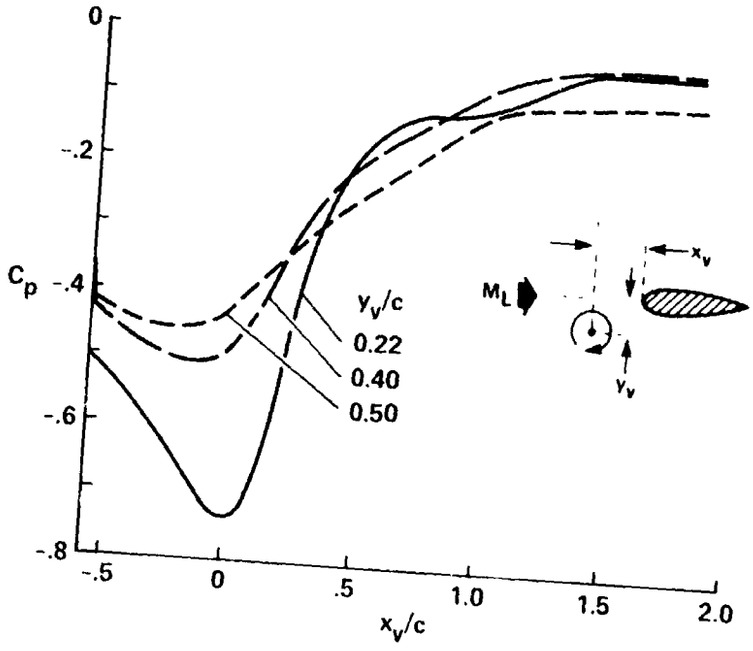

Figure 18. The effect of blade/vortex proximity on leading edge pressure variations: $M_L = 0.536$, $C_{LV} = 0.62$, $x/c = 0.02$, NACA 0012.